Title

Intracranial vessel wall segmentation with deep learning using a novel tiered loss function incorporating class inclusion.

Journal

Medical Physics, 49(11)

Authors

Zhou, Hanyue
Xiao, Jiayu
Li, Debiao
et al.

Publication Date

2022-11-01

DOI

10.1002/mp.15860

Peer reviewed

HHS Public Access

Author manuscript

Med Phys. Author manuscript; available in PMC 2023 November 01.

Published in final edited form as:

Med Phys. 2022 November ; 49(11): 6975–6985. doi:10.1002/mp.15860.

Intracranial Vessel Wall Segmentation with Deep Learning using a Novel Tiered Loss Function Incorporating Class Inclusion

Hanyue Zhou[1], **Jiayu Xiao**[2], **Debiao Li**[1,3], **Zhaoyang Fan**[2,4,5], **Dan Ruan**[1,6]

[1] Department of Bioengineering, University of California, Los Angeles, Los Angeles, CA 90095, USA

[2] Department of Radiology, University of Southern California, Los Angeles, CA 90033, USA

[3] Biomedical Imaging Research Institute, Cedars-Sinai Medical Center, Los Angeles, CA 90048, USA

[4] Department of Radiation Oncology, University of Southern California, Los Angeles, CA 90033, USA

[5] Department of Biomedical Engineering, University of Southern California, Los Angeles, CA 90089, USA and

[6] Department of Radiation Oncology, University of California, Los Angeles, CA 90095, USA

Abstract

Purpose: To develop an automated vessel wall segmentation method on T1-weighted intracranial vessel wall magnetic resonance images, with a focus on modeling the inclusion relation between the inner and outer boundaries of the vessel wall.

Methods: We propose a novel method that estimates the inner and outer vessel wall boundaries simultaneously, using a network with a single output channel resembling the level-set function height. The network is driven by a unique tiered loss that accounts for data fidelity of the lumen and vessel wall classes and a length regularization to encourage boundary smoothness.

Results: Implemented with a 2.5D UNet with a ResNet backbone, the proposed method achieved Dice similarity coefficients (DSC) in 2D of 0.925 ± 0.048, 0.786 ± 0.084, Hausdorff distance of 0.286 ± 0.436mm, 0.345 ± 0.419mm and mean surface distance (MSD) of 0.083 ± 0.037mm and 0.103 ± 0.032mm for the lumen and vessel wall, respectively, on a test set; compared favorably to a baseline UNet model that achieved DSC 0.924 ± 0.047, 0.794 ± 0.082, HD 0.298 ± 0.477mm, 0.394 ± 0.431mm, and MSD 0.087 ± 0.056mm, 0.119 ± 0.059mm. Our vessel wall segmentation method achieved substantial improvement in morphological integrity and accuracy compared to benchmark methods.

Conclusions: The proposed method provides a systematic approach to model the inclusion morphology and incorporate it into an optimization infrastructure. It can be applied to any

druan@mednet.ucla.edu .

DISCLOSURE OF CONFLICTS OF INTEREST

The authors have no relevant conflicts of interest to disclose.

application where inclusion exists among a (sub)set of classes to be segmented. Improved feasibility in result morphology promises better support for clinical quantification and decision.

Keywords

Vessel wall segmentation; deep learning; morphological inclusion; boundary length regularization; level-set methods

INTRODUCTION

Stroke is a leading cause of morbidity and mortality in the US and worldwide[1,2]. Intracranial atherosclerosis disease (ICAD), characterized by lipid deposition, inflammation, and remodeling in the artery vessel wall, remains a major risk factor for stroke occurrence. Magnetic resonance (MR) vessel wall imaging (VWI) is an emerging non-invasive technology to assist in ICAD evaluation, thanks to its high spatial resolution and superior dark-blood contrast[3]. Quantitative assessment of atherosclerotic lesions based on MR-VWI may provide valuable insights into the severity of ICAD[4]. Several morphological measurements, such as normalized wall index, arterial wall remodeling ratio, and plaque-to-wall contrast ratio, have been shown to be useful imaging surrogates for plaque burden quantification[5–9]. These measurements rely on accurate contouring of the vessel wall in a cross-sectional view.

Vessel wall contouring is typically performed manually and is subject to high inter- and intra- observer variations. These variations can induce high uncertainty on subsequent quantitative analysis on the small intracranial arteries. Moreover, with the advent of 3D VWI with large spatial coverage[10,11], the presence of multiple ICAD lesions in a patient may incur intensive labor cost and exacerbate human errors. These limitations and concerns call for an automated method to improve segmentation accuracy, consistency, and efficiency.

Conventional automated or semi-automated vessel wall segmentation methods applied to MR-VWI images are usually based on explicit model fitting. For example, the shape of a whole carotid vessel was approximated as elliptic, and was translated, deformed, and rotated iteratively to fit the outer vessel wall boundary[12]. In each iteration, the similarity of the ellipse to the outer wall boundary was evaluated with the average intensity gradient magnitude along the ellipse. The ellipse with the highest intensity gradient average was obtained as the final outer wall boundary. In addition to the 2D model, a 3D model has been investigated by deforming a 3D cylindrical non-uniform rational B-spline surface to fit the inner and the outer vessel wall boundary of a carotid artery[13]. A tube model was initialized by rings with pre-specified diameters and numbers of control points, and the control point locations were adjusted iteratively with signal intensities. The major disadvantages of these methods are the long computation time for iterative model fitting and the potential model misfit when the shape assumptions are violated.

As an alternative to the parametric approaches, level-set based methods can perform numerical computations of curves and surfaces on a fixed Cartesian grid and handle varying topology with ease[14]. Level-set based active contour approaches have been investigated to extract the lumen and outer wall boundaries by minimizing an energy function with

fidelity force to align boundary with high gradients, and regularization for smoothness on in-plane contour shape and consistency across adjacent slices[15]. Typical ordinary differential equation (ODE)-based level-set methods usually require long computation time.

Recent research has been utilizing deep neural networks to perform automated vessel wall segmentation, using either a multi-class or multi-label setting. The multi-class methods predict multiple mutually exclusive classes by the same number of output channels, usually with softmax activation in the last network layer. With this setting, Shi *et al.* proposed a 2D UNet to segment the intracranial vessel and reported Dice similarity coefficients (DSC) of 0.89 and 0.77 for the lumen and vessel wall, respectively[16]. In contrast, the semantic segmentation to predict in a multi-label setting can be overlapped, and each pixel can have multiple class memberships. The multi-label setting usually has sigmoid activation in the last network layer, where binary prediction is performed for each class. With this setting, a 2.5D UNet was developed to segment the lumen, whole vessel, and background for the carotid arteries, and achieved DSC of 0.96 and 0.97 for the lumen and whole vessel, respectively[17]. We recently proposed a 2.5D UNet++ model in a multi-label setting where a distance-transform approximated Hausdorff distance (HD) along with soft Dice was used to further improve segmentation accuracy[18].

While the reported DSC values were reasonably high, they only indicate a good overlap between the labeled and predicted class memberships, by treating the lumen and the whole vessel (or vessel wall) as separate classes without considering the intrinsic coupling that the lumen resides inside the entire vessel. In other words, the set of lumen pixels should be a proper subset of the whole vessel pixel set, and we use the word “inclusion” hereafter to indicate this concept. This is particularly a concern for deep learning methods as there is little control once the network is trained. In the intracranial arteries, the contrast of the outer vessel boundary may be low, and vessel shapes are more irregular due to tortuosity and frequent branching. As a result, existing networks have been observed to generate morphologically infeasible solutions, such as lumen pixels outside of the vessel, isolated pixel sets, and highly oscillatory pattern or peaky singularity on the boundary, as illustrated in Fig. 1.

Realizing the importance to account for inclusion morphology, Chen *et al.* proposed a carotid artery segmentation network in the polar coordinate system[19]. By converting MR-VWI images into a polar coordinate system using an estimated lumen center as the reference origin, the segmentation problem became a regression task where the distances from the lumen center to the lumen boundary and the whole vessel boundary along each radial direction were predicted. The segmentation convolutional neural network (CNN) contained a fully connected (FCN) layer to predict the polar coordinates for the lumen boundary and whole vessel boundary in t sampled polar directions.

DSCs of 0.961 and 0.860 were reported for the lumen and the vessel wall, respectively, compared to 0.922 and 0.774 from the conventional Cartesian coordinate system. It was claimed that performing segmentation in the polar system has the advantages of: 1) ensuring contour continuity when enforcing the distance from the lumen center to the predicted whole vessel boundary to be larger than that of the lumen boundary, and 2) easily differentiating

adjacent arteries from the artery to be segmented. A prerequisite for segmenting in the polar coordinate is a reliable definition of the centerline. A tracklet refinement algorithm was proposed for lumen center localization and centerline tracking to meet this requirement[19].

While this combination of centerline tracking and polar analysis for vessel wall may work well for the large carotid arteries, it is a lot more challenging to ensure a good automatic centerline for the much smaller intracranial vessels, whose signal and contrast strength could be low or disruptive even in angiography. In this study, we propose and develop a novel method to address the demand to account for topology inclusion with much relaxed requirement on "centerline" or origin definition. Our key contributions are: 1) inspired by the level-set methods idea we incorporate the inclusion relationship between the whole vessel and the lumen by level-set function heights; 2) we utilize a single-channel-output UNet structure to incorporate the inclusion relationship into an optimization infrastructure; 3) we propose a novel loss function for effective optimization with the network infrastructure between the predicted class membership and ground truth while regularizing the smoothness of the segmentation boundaries.

MATERIALS

Under IRB approval *Pro*00055925 on 05/30/2019, T1-weighted MR VWI from 80 patients diagnosed with ICAD were obtained for this study. The images were acquired with a whole-brain MR VWI protocol[11,20], using a 3-Tesla whole-body system (MAGNETOM Prisma; Siemens Healthcare, Erlangen, Germany) and a 64-channel head/neck coil (Siemens Healthcare). The images were acquired at an isotropic spatial resolution of 0.55 mm. The following four arterial segments including the one that involved the identified plaque were used for segmentation sample preparation: the intracranial internal carotid artery, the middle cerebral artery, the intracranial vertebral artery, and the basilar artery. 3D Slicer (version 4.11.0) was used to generate 30 contiguous 2D cross-sectional slices with 0.55 mm slice thickness and 0.1 mm in-plane resolution from each segment[21]. The "ground truth" lumen and vessel wall were labeled by an experienced radiologist using ITK-SNAP (version 3.8.0)[22]. For quality assurance purpose intra-observer labeling consistency was verified. The variability of vessel wall DSC was assessed to be 0.82±0.07 between two rounds of labeling by the same radiologist performed two weeks apart.

METHODS

We propose to account for the inclusion morphology with coupled level-set functions and using a deep neural network approach as the overall structure. In particular, we develop a network with a *single* output channel to infer the soft "tiered" memberships of the lumen, whole vessel, and background simultaneously, in sharp contrast to the typical multi-channel predictions in multi-class or multi-label settings. Fidelity is defined based on class agreement between the "ground truth" labels and the prediction derived from the level-set as in Eq. (6). The training cost is further regularized with penalty Eq. (7) and Eq. (9) to encourage smoothness of the network predicted value function and the vessel wall boundaries, respectively. Fig. 2. illustrates the general schema of the proposed method. We deploy a 2.5D UNet structure with ResNet backbone in our implementation. The 2.5D

structure takes three consecutive VWI slices with image size 128 × 128 as input, and outputs the class prediction for the middle slice. Vessel centerlines are as external input, and the VWI image slices are centered by the centerline with a field of view 12.8 × 12.8 mm^2.

Level-set Formulation

To encode inclusion, we consider the ordinal relations among various level-sets with respect to a single level-set function. Under a 2D setting, let $\phi(x) : R^2 \rightarrow R$ be a level-set function, the lumen and the whole vessel pixels are associated with:

$$\begin{aligned} &\Omega_{\text{lumen}}\{x : \phi(x) < \eta_1\}, \\ &\Omega_{\text{whole\_vessel}}\{x : \phi(x) < \eta_2\}. \end{aligned} \tag{1}$$

We take advantage of the simple relation that for $\eta_1 < \eta_2$, $\Omega_{\text{lumen}} \subset \Omega_{\text{whole\_vessel}}$ reflects the inclusion relationship. In this specific application, we may define the background as the complement of the larger set $\Omega_{\text{background}} = D - \Omega_{\text{whole\_vessel}}$, where $D \in R^2$ denotes the entire segmentation domain. Without loss of generality, we may set $\eta_1 = \frac{1}{3}$, $\eta_2 = \frac{2}{3}$. Fig. 3. illustrates the level-set idea.

The membership of a pixel $x \in R^2$ is obtained by taking the level-set function through a Heaviside function H:

$$\begin{cases} H(\eta_1 - \phi(x)) = 1, \ x \in \Omega_{\text{lumen}} \\ H(\eta_2 - \phi(x)) \cdot H(\phi(x) - \eta_1) = 1, \ x \in \Omega_{\text{vessel\_wall}} \\ H(\phi(x) - \eta_2) = 1, \ x \in \Omega_{\text{background}}, \end{cases} \tag{2}$$

where

$$H(x) = \begin{cases} 1, \ x \geq 0 \\ 0, \ x < 0; \end{cases} \tag{3}$$

which is then relaxed to a continuous differential sigmoid function $S(x) = \frac{1}{1 + e^{-x}}$ to generate a “soft membership” for each class given in Eq. (4).

The corresponding continuous probability-like relaxation of the network predicted value function y to y' is given by

$$\begin{cases} y'_{\text{lumen}} = S(\eta_1 - y), \\ y'_{\text{vessel\_wall}} = S(\eta_2 - y) \cdot S(y - \eta_1), \\ y'_{\text{background}} = S(y - \eta_2). \end{cases} \tag{4}$$

UNet with ResNet Backbone Structure

A 2.5D UNet model with ResNet backbone is used for level-set inference[23,24], as demonstrated in Fig. 4. The convolution blocks in the UNet model each consists of one

convolution layer followed by batch normalization, and another convolution layer. With a ResNet backbone, a skip-connection is inserted after the input of each convolution block and is passed through a 1 × 1 convolution to add the feature of the previous layer to the last layer of a convolution block. The network has a single channel output via a 1 × 1 convolution layer with sigmoid activation. This single-channel prediction maps each pixel's value to its corresponding class membership.

Training Objective

The deep neural network is trained to minimize an objective function consisting of three terms: a fidelity term to match the derived level-sets with the training labels and two regularization terms to encourage smoothness for the network predicted value function and the class boundaries, respectively.

The overall loss function is a summation of the three terms weighted by regularization hyperparameters λ and γ:

$$\mathscr{L} = \mathscr{L}^{\text{Fidelity}} + \lambda \mathscr{L}^{\text{Smooth}} + \gamma \mathscr{L}^{\text{Length}} \tag{5}$$

The fidelity term defines the agreement between the predicted and the given labels using soft Dice criterion for the lumen, vessel wall, and background classes.

$$\mathscr{L}^{\text{Fidelity}} = \sum_{c} (1 - \frac{1}{N} \sum_{n = 1, \ldots, N} \frac{2 p_{n,c} y'_{n,c}}{p^2_{n,c} + y'^2_{n,c}}), \tag{6}$$

where $y'_{n,c}$ and $p_{n,c}$ are the soft prediction from Eq. (4) and the "ground truth" labels for the nth pixel of class c = lumen, vessel wall, background, respectively. N is the total number of pixels in a batch.

To encourage clear and robust differentiation between the adjacent classes, i.e., lumen vs. vessel wall, and vessel wall vs. background, we introduce an l_2 norm to the gradient of the network output y to prevent oscillation and promote stable region-wise homogeneous membership.

$$\mathscr{L}^{\text{Smooth}} = \frac{1}{N} \sum \| \nabla y \|^2, \tag{7}$$

where ∇ is the spatial differential operator:

$$\nabla y = \left(y_{i+1,j} - y_{i,j},\ y_{i,j+1} - y_{i,j} \right), \tag{8}$$

with i and j indexing over the horizontal and vertical axes in 2D images.

Penalizing the magnitude of the gradient encourages smooth transitions in y, and has two important consequences (1) it leads to congruent connected labeled regions upon inference, and (2) for any ray starting from the lumen, smooth membership transition ensures a good chance of encountering a decent-sized vessel wall class before entering the background class, as illustrated by the example profile view in Fig. 3 (a).

As in active contour approaches, we further impose a length penalty based on total variation (TV) on the vessel wall class to reduce the roughness of the inner and outer boundaries of the vessel wall[25,26]:

$$\mathscr{L}^{\text{Length}} = \frac{1}{N}\sum \left\| \nabla y'_{\text{vessel\_wall}} \right\|. \tag{9}$$

Assessment Criteria

Conventional measure—The primary goal of segmentation is label agreement and it is typical to measure segmentation performance by calculating DSC, 95 percentile HD (HD 95), and mean surface distance (MSD) from the prediction to the ground truth. DSC measures the globally overlapping degree, while HD and MSD measure the biggest and the averaged point-wise matching discrepancy, between the prediction and the ground truth, respectively.

Clinical measure—The clinically relevant quantification feature - the lumen and vessel wall area as well as normalized wall index (NWI) are also adopted as measures to match a common clinical practice. NWI is defined as $\frac{A_{\text{vessel\_wall}}}{A_{\text{vesgel\_wall}} \cup A_{\text{lumen}}}$, where A denotes area. NWI ranges from 0 to 1, and with a higher value indicating a heavier plaque burden. We report the mean absolute error (MAE) of the NWI, lumen area (A_{lumen}), and vessel wall area ($A_{\text{vessel\_wall}}$), where area is measured in pixels.

Geometric measure—To assess segmentation quality, the MAE of the inner and outer boundary length (L) of the vessel wall, as well as the mean error (ME) of the lumen area and vessel wall area are reported in pixels. We further propose two metrics to measure the geometric integrity. To quantify the existence of isolated pixels as in Fig. 1.(b), connected component analysis is applied and the summed area of small islands (denoted as N_{Iso}) is reported in pixels. The numbers of violation of inclusion as in Fig. 1.(a) is measured using membership gradient:

$$N_{\text{V}} = \sum \text{I}\left\{ \nabla y^d > 1 \right\}, \tag{10}$$

where **I** denotes the indicator function, and y^d is the categorized membership which has the value of 2 for lumen pixels, 1 for vessel wall, and 0 for background. N_V counts the amount of lumen pixels that directly connect to the background pixels.

The mean and the standard deviation of each measure above are reported for a test set. One-sided paired t-tests with $p < 0.05$ are applied between the measure achieved by each method in comparison and the best measure, for each class, where applicable.

EXPERIMENTS

We randomly split the recorded 80 patients into 74 : 3 : 3 for training, validation, and testing, respectively. Again, each patient was associated with four segments, and each segment had 30 2D cross-sectional image slices. Metrics and statistics were calculated slice-wise.

In our implementation of UNet with ResNet backbone, the depth of the UNet model was four, and the base number of channels was 32. The learning rate for all segmentation models was 10^{-4} for a total of 50 epochs, with Adam optimizer and a batch size of 64. The regularization hyperparameter λ was 0.1 and γ was 0.5, all tuned with respect to the validation performance.

The proposed method was compared with the conventional multi-label segmentation[17], and the polar-coordinated segmentation methods[26], both qualitatively and quantitatively.

The benchmark multi-label method utilized the same 2.5D UNet structure with ResNet backbone as the proposed method, with three output channels representing the prediction of the lumen, whole vessel, and background, respectively. The training objective was the sum of soft Dice across these three independent classes, regularized with length penalty for the lumen and the whole vessel classes, as in Eq. (9).

To compare with segmentation in polar coordination system[26], the images were first resampled to 256 × 256 from 128 × 128 with nearest neighbor interpolation before polar conversion, and the model predictions were eventually converted back to the Cartesian coordinates. The same segmentation network structure as the proposed method with 128 × 128 × 3 input size was used, and an FCN with $2t = 256$ nodes was attached to the last layer of the UNet. Specifically, the prediction of the multi-label and the proposed tiered models was upsampled to 256 × 256 to maintain the same dimension as the results by the polar method and also to achieve a smoother segmentation.

The polar intersection over union (IoU) loss function was used for network training for the polar method as in Eq. (11)[27]. Manually extracted centerlines were used as the polar origin instead of the iteratively refined centerline as in[19] to alleviate the challenge of fully automated centerline tracking for small intracranial vessels. The samples whose labels cannot be polar converted were removed from the training set, and two examples of such samples are illustrated in the Results Section Fig. 6.

$$\text{Polar IoU Loss} = \log \frac{\sum_{i=1}^{t} \min(d,\ d')}{\sum_{i=1}^{t} \max(d,\ d')}, \tag{11}$$

where d and d' are the ground truth and the predicted coordinates in the polar system, respectively, along each of the t directions.

Ablation study was performed to assess the contribution of each component in the overall loss function of the proposed tiered method, where the weighting hyperparameters were the same as the proposed method.

RESULTS

Method Comparisons

Fig. 5. illustrates the qualitative results of the conventional multi-label method, the polar segmentation method, and the proposed tiered method. It can be observed that

the proposed tiered method achieved smoother boundaries and better resemblance to the ground truth manual segmentation, compared to other methods. The method helped to alleviate the overestimation of the vessel wall area compared to the conventional multi-label segmentation method, and achieved a better preservation of morphology than the polar method when the segmented shapes deviated further from regular circles, shown from the column (d) where the segmentation resembled a union of two circles, despite an over-regulated vessel wall shaping compared to the conventional multi-label method.

Table I reports the quantitative performance of the above methods for comparison. The tiered method generally achieved the best measure across metrics among all the methods. The substantial reduction in the MAE of the NWI and areas indicates that the morphological improvement offered by the tiered approach has manifested favorably into quantitative clinical endpoints.

Table II reports the geometric integrity across the testing set. The results show that none of the method had the problem of lumen pixels directly connecting to the background as a violation of inclusion for our specific randomly selected test-set. However, the proposed tiered method achieved substantially less isolated pixels of vessel wall compared to the conventional multi-label method. The proposed method also achieved the smallest MAE of boundary lengths and alleviated the under-estimation of lumen area and the over-estimation of vessel wall area of the other two methods.

Fig. 6. shows two examples where the polar conversion encountered problems. These types of samples were removed from the training set, and their inference results were illustrated. Despite maintaining a good geometric integrity, the results were not very close in morphology to the “ground truth” segmentation and image cues, as the relatively complex morphology with tortuous boundaries was not seen during training.

Ablation Studies

We compared the results obtained by using the loss function of 1) only the soft Dice loss $\mathscr{L}^{\text{Fidelity}}$, 2) soft Dice as the fidelity and the smooth loss term $\mathscr{L}^{\text{Smooth}}$, 3) soft Dice and the length penalty term $\mathscr{L}^{\text{Length}}$, and 4) the proposed soft Dice together with the smooth loss and length penalty. Fig. 7. illustrates the qualitative results of the ablation studies. The results show that the $\mathscr{L}^{\text{Smooth}}$ was essential for reducing holes in the segmentation and regularizing morphology. The $\mathscr{L}^{\text{Length}}$ term further regulated the morphology, and helped smooth out the segmentation boundaries and reduce small isolated pixel sets occur in the background. The quantitative results in Table III show that the proposed method generally achieved the best performance, and each term was critical for the method formulation.

DISCUSSIONS

DSC, HD, and MSD are adopted as metrics for the purpose of performing comparison with benchmark methods in literature. They do not fully reveal the intended accuracy for clinical endpoints in vessel segmentation in failing to capture morphological feasibility.

With two regularization terms to encourage the smoothness of the membership transition and segmentation boundaries, the proposed tiered method achieved substantially better morphological feasibility than the conventional multi-label method without much compromising typical segmentation performance in DSC, HD, and MSD. The clinically relevant plaque assessment - NWI, A_{lumen}, and $A_{\text{vessel\_wall}}$ also enjoyed substantial improvements, promising advantages in downstream clinical tasks.

In comparison, compromised segmentation performance was observed with the polar-system method[19], possibly caused by replacing the soft Dice loss with the polar IoU as the objective to maintain geometric integrity. Originally proposed to segment carotid arteries with larger sizes and more regular and circular/elliptical vessel shapes, the polar method was challenged with the finer and more torturous intracranial cases, which was the focus in our study. A related observation was that the finer structure in intracranial vessels also demanded more numerical stability during coordinate conversions: the polar method required meticulous definition of centerline or image center to maintain ray-wise convexity. While the training samples with out-of-lumen center or non-convex vessel shapes may be removed with additional adjudication and manual examination, it is impractical to remove such samples at inference time, which eventually gives rise to system breakdown or erroneous results. A derived benefit of our method's robustness in being compatible with all cases is the avoidance of selective removal so that the network can receive a broad exposure without artificial bias.

Correlation exists between adjacent slices and strictly speaking the covariance needs to adjusted, and correspondingly the threshold for p-value. In this work, the statistical comparisons are intended to elucidate that the proposed method achieved improved morphological fidelity without compromising the performance w.r.t the commonly used metrics such as DSC and MSD.

It is worth noting that the geometric inclusion is not a consequence of the native level-set representation, where a multi-phase one uses either $n - 1$ or $\log_2(n)$ level-set functions to represent n phases and allows each region to evolve[28]. When applied to vessel segmentation problems, these methods handle the inner and outer vessel wall boundaries separately without accounting for their relative placement[15,29]. The logic addition and subtraction used in the composite multiphase may provide some adjacency constraint but is insufficient to reflect the enclosing vessel "ring" on lumen[28], unlike the proposed tiered level-set derived from a single value function. In addition to the morphological benefits with tiered level-sets, the proposed method inherits efficiency advantage from the deep learning with fast inference, compared to typical level-set methods solved with iterations.

Our general method with morphological regularization is compatible with segmentation model of any dimensionality, including 2D and 3D. One needs to be mindful in modifying the level-set functional formulation to reflect the inclusion relation in the cross-sectional with a possible reasonably controlled tilting angle. The current method requires tuning two hyperparameters for balancing regularization weights. We are actively investigating alternative regularization schemes to either simplify the design or learn the hyperparameters[30]. Furthermore, we are working on extending the proposed method to

segment the entire vessel structure within the brain to further take advantage of the level-set's flexibility in handing topology transitions and coping with bifurcations.

While we have demonstrated the efficacy of our method with controlled data and expect the methodology of morphology regularization to generalize, it is also important to realize that its efficacy and the level of potential improvement could have a strong dependency on the use cases, including but not limited to the anatomy structure site of study, imaging platform, imaging and contouring protocols.

CONCLUSIONS

We have proposed a novel and effective segmentation method based on deep neural networks that particularly preserves the inclusion relationship between the lumen and the whole vessel. Our proposed method relates the classes intrinsically with a function whose value provides an ordinal indication for the tiered class membership. The proposed method have achieved better segmentation accuracy and morphology both qualitatively and quantitatively compared to benchmark methods. The proposed method can be adopted to any applications that have similar inclusive settings between classes to generate morphological feasible segmentation solutions, and the improved morphology promises better evaluation support.

ACKNOWLEDGMENT

This work is supported in part by NIH/NHLBI R01 HL147355. HZ and DR would like to acknowledge the UCLA Radiation Oncology Department for infrastructure support.

DATA AVAILABILITY STATEMENT

The data are not publicly available due to privacy or ethical restrictions.

REFERENCES

1. Ahmad Farida B, Anderson Robert N The Leading Causes of Death in the US for 2020 JAMA. 2021;325:1829–1830. [PubMed: 33787821]
2. Murphy Stephen JX, Werring David J Stroke: causes and clinical features Medicine. 2020;48:561–566. [PubMed: 32837228]
3. Bodle Jeffrey D, Edward Feldmann, Swartz Richard H, Zoran Rumboldt, Truman Brown, Turan Tanya N High-Resolution Magnetic Resonance Imaging Stroke. 2013;44:287–292. [PubMed: 23204050]
4. Song Jae W, Athanasios Pavlou, Jiayu Xiao, Kasner Scott E, Zhaoyang Fan, Messé Steven R Vessel Wall Magnetic Resonance Imaging Biomarkers of Symptomatic Intracranial Atherosclerosis: A Meta-Analysis Stroke. 2020;52:193–202. [PubMed: 33370193]
5. Jiayu Xiao, Padrick Matthew M, Tao Jiang, et al. Acute ischemic stroke versus transient ischemic attack: Differential plaque morphological features in symptomatic intracranial atherosclerotic lesions Atherosclerosis. 2021;319:72–78. [PubMed: 33486353]
6. Ye Qiao, Zeeshan Anwar, Jarunee Intrapiromkul, et al. Patterns and Implications of Intracranial Arterial Remodeling in Stroke Patients Stroke. 2016;47:434–440. [PubMed: 26742795]
7. Ye Qiao, Eliseo Guallar, Suri Fareed K, et al. MR imaging measures of intracranial atherosclerosis in a population-based study Radiology. 2016;280:860–868. [PubMed: 27022858]

8. Jiayu Xiao, Shlee Song, Konrad Schlick, et al. Disparate trends of atherosclerotic plaque evolution in stroke patients under 18-month follow-up: a 3D whole-brain magnetic resonance vessel wall imaging study The Neuroradiology Journal. 2021:197140092110269.
9. Fang Wu, Qingfeng Ma, Haiqing Song, et al. Differential features of culprit intracranial atherosclerotic lesions: A whole-brain vessel wall imaging study in patients with acute ischemic stroke Journal of the American Heart Association. 2018;7.
10. Ye Qiao, Steinman David A, Qin Qin, et al. Intracranial arterial wall imaging using three-dimensional high isotropic resolution black blood MRI at 3.0 Tesla Journal of Magnetic Resonance Imaging. 2011;34:22–30. [PubMed: 21698704]
11. Zhaoyang Fan, Qi Yang, Zixin Deng, et al. Whole-brain intracranial vessel wall imaging at 3 Tesla using cerebrospinal fluid–attenuated T1-weighted 3D turbo spin echo Magnetic Resonance in Medicine. 2017;77:1142–1150. [PubMed: 26923198]
12. Adame Isabel M, Geest Rob J, Wasserman Bruce A, Mona Mohamed, Reiber Johan Hans C, Lelieveldt Boudewijn PF Automatic plaque characterization and vessel wall segmentation in magnetic resonance images of atherosclerotic carotid arteries in Medical Imaging 2004: Image Processing (Michael Fitzpatrick J., Milan Sonka, eds.);5370:265–273International Society for Optics and PhotonicsSPIE 2004.
13. Ronald Klooster, Koning Patrick JH, Alizadeh Dehnavi Reza, et al. Automatic lumen and outer wall segmentation of the carotid artery using deformable three-dimensional models in MR angiography and vessel wall images Journal of Magnetic Resonance Imaging. 2012;35:156–165. [PubMed: 22031339]
14. Stanley Osher, Fedkiw Ronald P Level Set Methods: An Overview and Some Recent Results Journal of Computational Physics. 2001;169:463–502.
15. Yan Wang, Florent Seguro, Evan Kao, et al. Segmentation of lumen and outer wall of abdominal aortic aneurysms from 3D black-blood MRI with a registration based geodesic active contour model Medical Image Analysis. 2017;40:1–10. [PubMed: 28549310]
16. Feng Shi, Qi Yang, Xiuhai Guo, et al. Intracranial Vessel Wall Segmentation Using Convolutional Neural Networks IEEE Transactions on Biomedical Engineering. 2019;66:2840–2847. [PubMed: 30716027]
17. Jiayi Wu, Jingmin Xin, Xiaofeng Yang, et al. Deep morphology aided diagnosis network for segmentation of carotid artery vessel wall and diagnosis of carotid atherosclerosis on black-blood vessel wall MRI Medical Physics. 2019;46:5544–5561. [PubMed: 31356693]
18. Hanyue Zhou, Jiayu Xiao, Zhaoyang Fan, Dan Ruan Intracranial Vessel Wall Segmentation For Atherosclerotic Plaque Quantification in 2021 IEEE 18th International Symposium on Biomedical Imaging (ISBI):1416–1419 2021.
19. Li Chen, Jie Sun, Gador Canton, et al. Automated Artery Localization and Vessel Wall Segmentation Using Tracklet Refinement and Polar Conversion IEEE Access. 2020;8:217603–217614. [PubMed: 33777593]
20. Qi Yang, Zixin Deng, Xiaoming Bi, et al. Whole-brain vessel wall MRI: A parameter tune-up solution to improve the scan efficiency of three-dimensional variable flip-angle turbo spin-echo Journal of Magnetic Resonance Imaging. 2017;46:751–757. [PubMed: 28106936]
21. Ron Kikinis, Pieper Steve D, Vosburgh Kirby G 3D Slicer: A Platform for Subject-Specific Image Analysis, Visualization, and Clinical Support in Intraoperative Imaging and Image-Guided Therapy:277–289Springer New York 2014.
22. Yushkevich Paul A, Joseph Piven, Cody Hazlett Heather, et al. User-guided 3D active contour segmentation of anatomical structures: Significantly improved efficiency and reliability NeuroImage. 2006;31:1116–1128. [PubMed: 16545965]
23. Olaf Ronneberger, Philipp Fischer, Thomas Brox U-Net: Convolutional Networks for Biomedical Image Segmentation CoRR. 2015;abs/1505.0.
24. Kaiming He, Xiangyu Zhang, Shaoqing Ren, Jian Sun Deep residual learning for image recognition Proceedings of the IEEE Computer Society Conference on Computer Vision and Pattern Recognition. 2016;2016-Decem:770–778.
25. Vogel CR, Oman ME Iterative methods for total variation denoising SIAM Journal of Scientific Computing. 1996;17:227–238.

26. Xu Chen, Williams Bryan M, Vallabhaneni Srinivasa R, Gabriela Czanner, Rachel Williams, Yalin Zheng Learning active contour models for medical image segmentation Proceedings of the IEEE Computer Society Conference on Computer Vision and Pattern Recognition. 2019;2019-June:11624–11632.

27. Enze Xie, Peize Sun, Xiaoge Song, et al. PolarMask: Single Shot Instance Segmentation with Polar Representation CoRR. 2019;abs/1909.13226.

28. Vese Luminita A, Chan Tony F A Multiphase Level Set Framework for Image Segmentation Using the Mumford and Shah Model * International Journal of Computer Vision. 2002;50:271–293.

29. Ukwatta E, Awad J, Ward AD, et al. Three-dimensional ultrasound of carotid atherosclerosis: Semiautomated segmentation using a level set-based method Medical Physics. 2011;38:2479–2493. [PubMed: 21776783]

30. Helen Victoria A, Maragatham G Automatic tuning of hyperparameters using Bayesian optimization Evolving Systems. 2021;12:217–223.

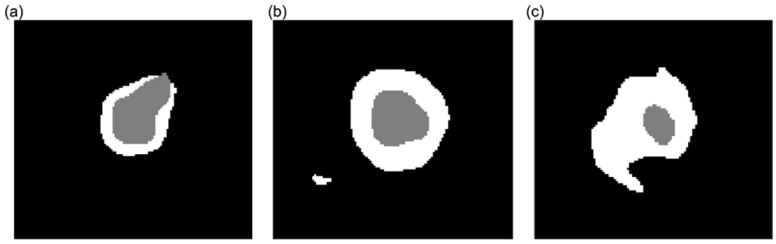

FIG. 1:
Morphologically infeasible examples of vessel wall segmentation generated by a naïve multi-label 2.5D UNet model: (a) lumen pixels outside of the vessel, (b) isolated pixel sets, and (c) highly oscillatory boundary.

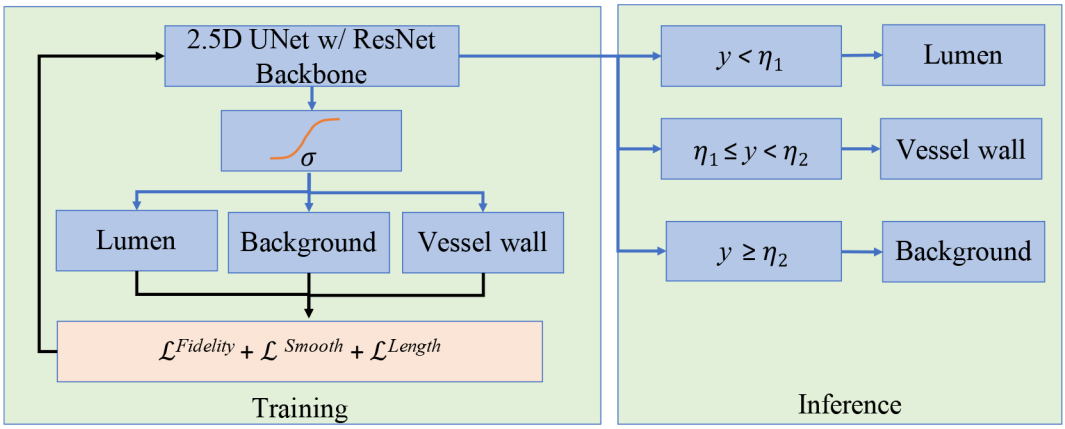

FIG. 2:

Schema of the proposed method: the training objective is the weighted sum of three loss terms: the fidelity on soft Dice $\mathscr{L}^{\text{Fidelity}}$ as Eq. (6), the $L2$-norm of the network predicted value function gradient $\mathscr{L}^{\text{Smooth}}$ as Eq. (7), and the total variation-based length penalty $\mathscr{L}^{\text{Length}}$ as Eq. (9) on the inner and outer vessel wall boundaries; the inference process simply maps the network output y into the predicted classes according to its values in the tier system.

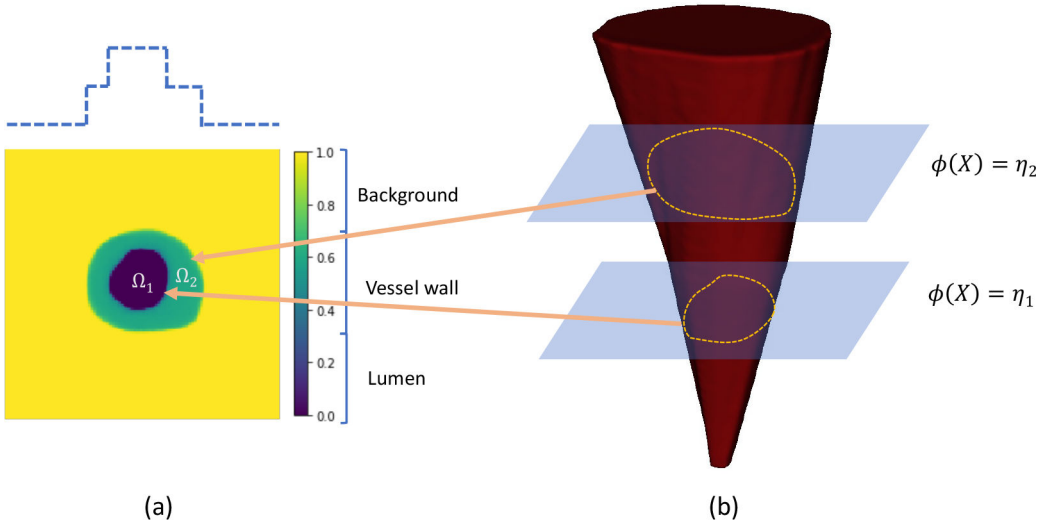

FIG. 3:

Illustration of level-set scheme: (a) is the output level-set map from the segmentation neural network: Ω_1 denotes the lumen, Ω_2 is the vessel wall, and $D - (\Omega_1 \cup \Omega_2)$ is the background. The dashed blue line illustrates the change of level-set function height with a ray starts from the background and encounters the vessel wall and lumen subsequently and goes back to the background. (b) is the illustration of the level-set function of the whole vessel and the lumen.

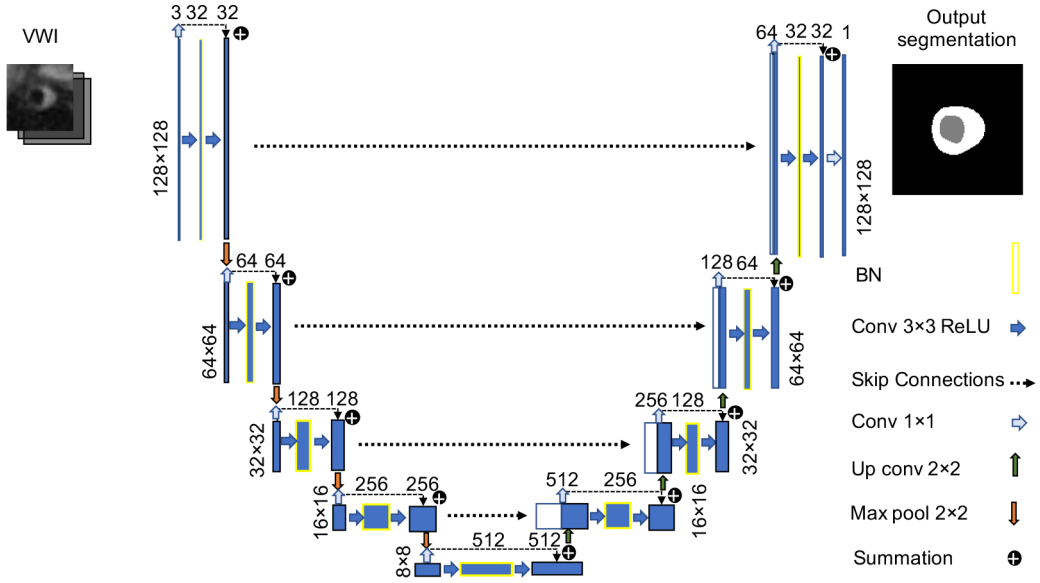

FIG. 4:

Illustration of the segmentation neural network: a skip-connection is inserted in each convolution block. Consecutive VWI slices are input to the network and a single-channel prediction of the background (black), lumen (gray), and the vessel wall (white) is output via sigmoid activation for the middle slice.

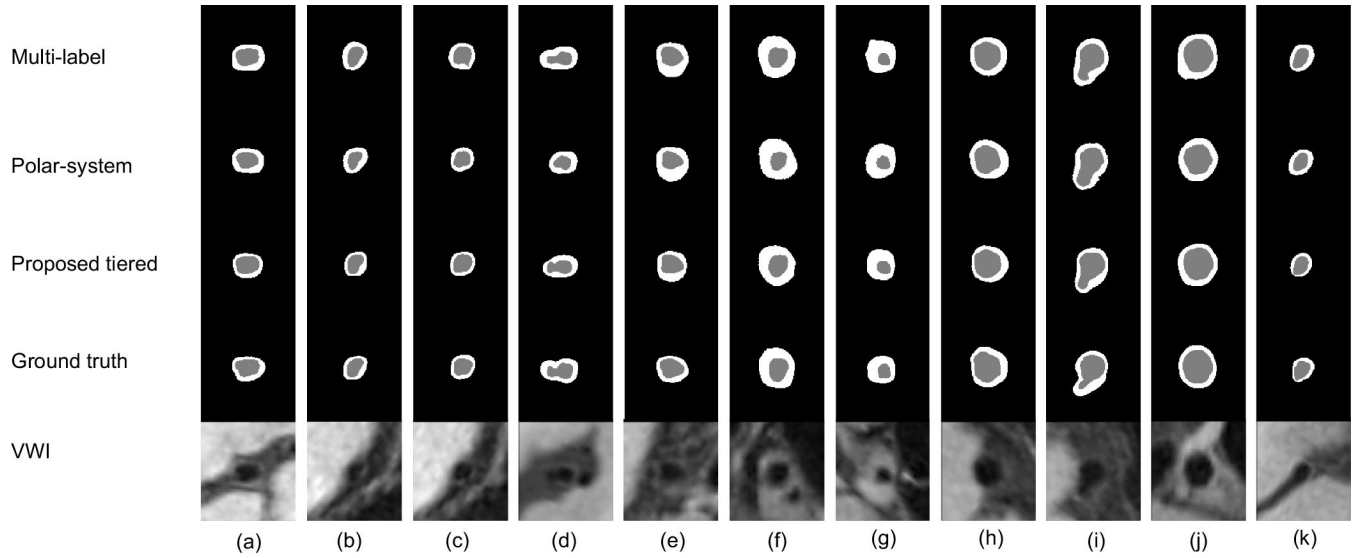

FIG. 5:

Qualitative visualization: each column is an example slice, and each row on the top panel corresponds to a different segmentation method corresponding to the cross-sectional vessel wall image on the bottom. The colors gray, white, and black indicate the lumen, vessel wall, and background, respectively.

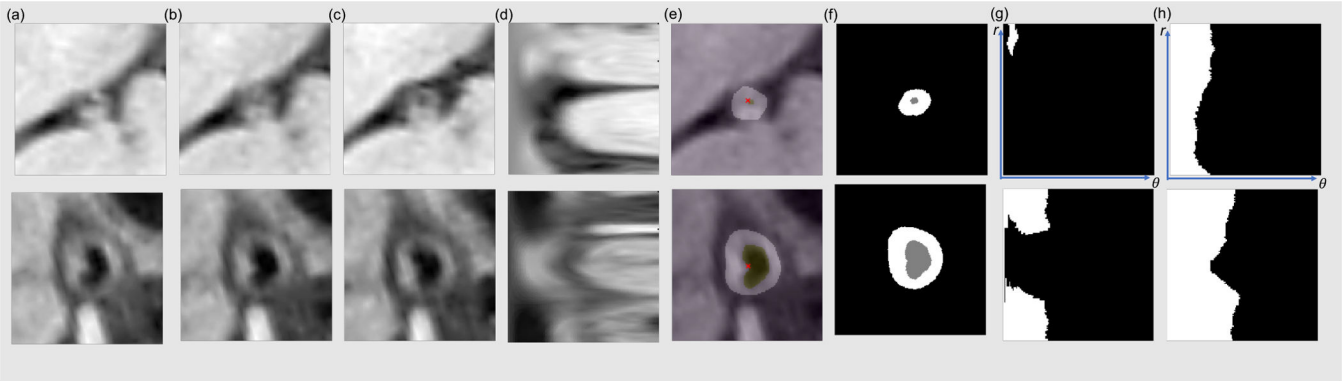

FIG. 6:

Two example slices in two rows where polar conversion is not applicable. (a),(b),(c): three consecutive VWI slices; (d): polar conversion of the middle slice (b); (e): ground truth lumen (yellow) and vessel wall (white) of (b), the red crossing shows the location of the image center (or polar origin); (f): the predicted labels by the polar method; (g): polar-converted ground truth lumen segmentation of (b); (h): polar-converted ground truth whole vessel segmentation of (b). The first example shows that when the lumen area is too small and the pre-detected lumen center (image center) is outside of the lumen area, the polar method encounters multiple intersections with the vertical axis. The second example shows that a non-convex shape leads to problems in polar conversion, as a line radiates from a detected lumen center can encounter multiple points on the segmentation boundary.

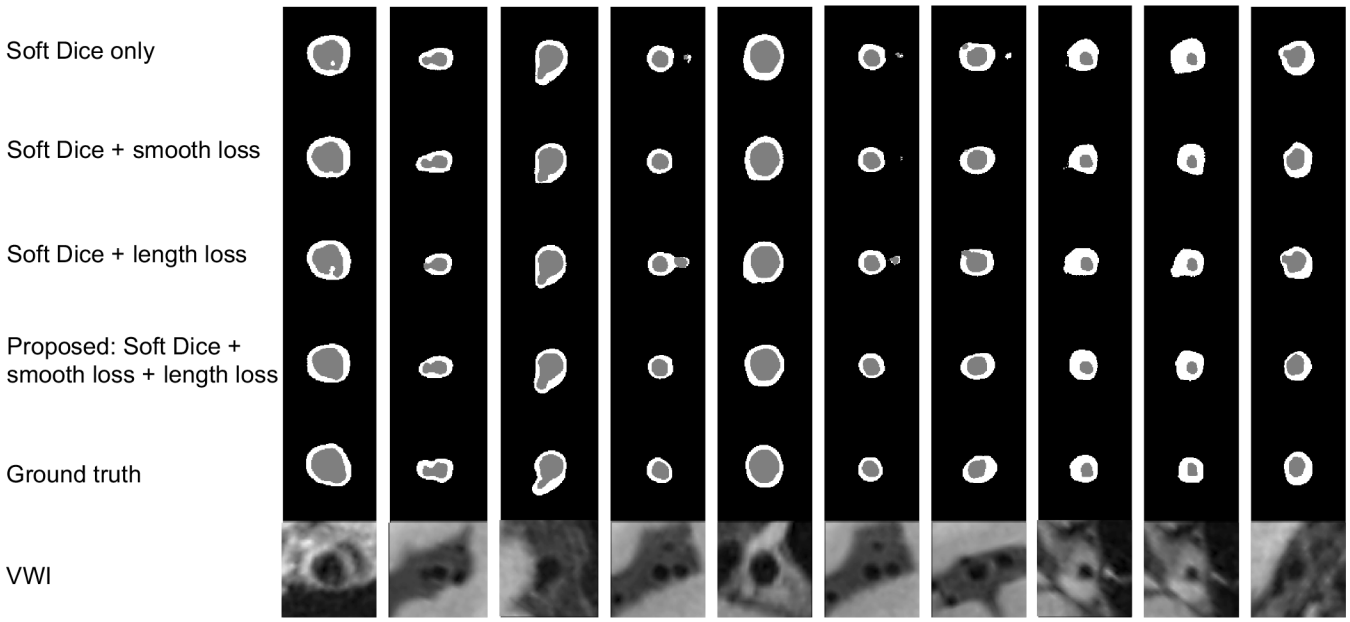

FIG. 7:

Ablation studies: each column is an example slice, and each of the first four rows is a different loss function. The proposed method achieves the best and smoothest shaping compared to with other objective alternatives, and thus each term is critical to the proposed loss function. Gray is the lumen, white the vessel wall, and black the background.

TABLE I:

Model Comparison in Conventional and Clinical Measures

Input/Class/Metric		DSC	HD_95 (mm)	MSD (mm)	A_MAE	NWI_MAE
Conventional multi-label segmentation	Lumen	0.924 ± 0.047	0.298 ± 0.477	0.087 ± 0.056	273.0 ± 357.5	0.065 ± 0.028 *
	Vessel Wall	**0.794 ± 0.082**	0.394 ± 0.431 *	0.119 ± 0.059 *	600.5 ± 476.5 *	
Polar-system segmentation	Lumen	0.893 ± 0.053 *	0.643 ± 0.703 *	0.233 ± 0.103 *	466.8 ± 400.9 *	0.077 ± 0.035 *
	Vessel Wall	0.781 ± 0.079 *	0.698 ± 0.609 *	0.233 ± 0.070 *	554.7 ± 460.7 *	
Proposed tiered segmentation	Lumen	**0.925 ± 0.048**	**0.286 ± 0.436**	**0.083 ± 0.037**	**257.6 ± 325.9**	0.050 ± 0.015
	Vessel Wall	0.786 ± 0.084 *	**0.345 ± 0.419**	**0.103 ± 0.032**	**490.6 ± 387.5**	

* one-sided t-test with $p < 0.05$, and bold numbers denote the best measure for each class across methods. The image size is 256 × 256.

TABLE II:

Model Comparison in Geometric Measures

Input/Class/Metric		A	A_ME	L	L_MAE	N_{Iso}	N_V
Conventional multi-label segmentation	Lumen	2810 ± 1357	−138.2 ± 428.0	227.4 ± 55.13	13.15 ± 23.83 *	4.015 ± 40.82 *	0
	Vessel Wall	3361 ± 1098	454.5 ± 617.3	335.4 ± 59.99	18.96 ± 22.44		
Polar-system segmentation	Lumen	2490 ± 1263	−458.1 ± 410.8	233.8 ± 60.67	13.34 ±18.61 *	**0**	0
	Vessel Wall	3274 ± 1169	367.5 ± 620.4	350.1 ± 67.37	29.18 ± 20.69 *		
Proposed tiered segmentation	Lumen	2933 ± 1397	−15.45 ± 415.1	231.5 ± 55.17	**12.37 ± 23.26**	0.050 ± 0.873	0
	Vessel Wall	2627 ± 1035	−279.1 ± 559.4	318.8 ± 62.34	**15.32 ± 22.54**		

* one-sided t-test with $p < 0.05$, and bold numbers denote the best measure for each class across methods. For the length measure L, lumen denotes the inner boundary, and vessel wall denotes the outer boundary for simplicity. The image size is 256 × 256.

TABLE III:

Ablation Studies

Input/Class/Metric		DSC	HD_95 (mm)	MSD (mm)	NWI_MAE
Soft Dice only	Lumen	0.924 ± 0.048	0.332 ± 0.539 *	0.091 ± 0.062 *	0.0651 ± 0.0260 *
	Vessel Wall	0.791 ± 0.085	0.402 ± 0.454 *	0.123 ± 0.062 *	
Soft Dice + smooth loss	Lumen	0.925 ± 0.046	0.289 ± 0.440	0.085 ± 0.040	0.0504 ± 0.0163
	Vessel Wall	**0.795 ± 0.080**	0.359 ± 0.429 *	0.106 ± 0.038 *	
Soft Dice + length loss	Lumen	0.925 ± 0.047	0.327 ± 0.506 *	0.096 ± 0.090 *	0.0503 ± 0.0148
	Vessel Wall	0.793 ± 0.078	0.370 ± 0.426	0.109 ± 0.054 *	
Soft Dice + smooth loss + length loss	Lumen	**0.925 ± 0.048**	**0.286 ± 0.436**	**0.083 ± 0.037**	**0.0498 ± 0.0146**
	Vessel Wall	0.786 ± 0.084 *	**0.345 ± 0.419**	**0.103 ± 0.032**	

* one-sided t-test with $p < 0.05$, and bold numbers denote the best measure for each class across all methods.